Model-Free Predictive Current Control of PMSM Using Modified Extended State Observer

Zixuan Liu, *Student Member, IEEE*, Xiaoyan Huang, *Member, IEEE*, Qichao Hu, Geng Yang, *Member, IEEE*, Yunchong Wang, *Member, IEEE*, and Jianxin Shen, *Senior Member, IEEE*

***Abstract*—This article proposes a modified model-free predictive current control (M-MFPCC) integrated with a modified extended state observer (MESO). The goal is to reduce torque ripple and improving current distortion caused by inverter nonlinearity and other system disturbances. The disturbances are precisely observed with unity gain and zero phase delay. Adaptive gain updating of the proposed observer is implemented to track the frequency of the disturbance and sustain the noise suppression performance under various operating conditions. The proposed M-MFPCC can eliminate the high frequency harmonic disturbances without requiring additional information about inverter nonlinearity or necessitating extra parameter tuning. Experimental results confirm the proposed method's efficacy in suppressing current Total Harmonic Distortion (THD) and torque ripple under a variety of load conditions.**

***Index Terms*—Inverter nonlinearity, model-free predictive current control (MFPCC), permanent magnet synchronous machines, ultralocal model.**

NOMENCLATURE

R_s	Stator resistance.
L_d, L_q	dq-axis inductance.
ψ_f	Rotor flux linkage.
ω_e, θ_e	Rotor electronical speed and rotor position.
u_d, u_q	dq-axis voltages.
u_d^*, u_q^*	dq-axis voltage references.
i_d, i_q	dq-axis stator currents.
i_d^*, i_q^*	dq-axis stator currents references.
P_n	Motor pole numbers.
T_e	Motor torque.
f_d, f_q	dq-axis disturbance.
f_d', f_q'	dq-axis un-modeled disturbance.
ω_b	Bandwidth of the ESO.
v_d, v_q	dq-axis inverter nonlinearity voltage error.
v_a, v_b, v_c	Three phase inverter nonlinearity voltage error.
v_{err}	Theoretical value of the inverter voltage error.
h	High frequency disturbance.
ω_h, A_h, ϕ_h	Angular speed, amplitude and phase of the high-frequency disturbance.

Received 13 April 2024; revised 12 August 2024; accepted 4 October 2024. Date of publication 8 October 2024; date of current version 12 December 2024. This work was supported in part by the Key R&D Plan Projects in Zhejiang Province under Grant 2022C01001 and in part by the Fundamental Research Funds for the Zhejiang Provincial Universities under Grant 226-2023-00031. Recommended for publication by Associate Editor R. Kennel. *(Corresponding author: Xiaoyan Huang.)*

The authors are with the Zhejiang Provincial Key Laboratory of Electrical Machine Systems, College of Electrical Engineering, Zhejiang University, Hangzhou 310027, China (e-mail: eelzx@zju.edu.cn; xiaoyanhuang@zju.edu.cn; yanggeng@zju.edu.cn; j_x_shen@zju.edu.cn).

Color versions of one or more figures in this article are available at https://doi.org/10.1109/TPEL.2024.3476318.

Digital Object Identifier 10.1109/TPEL.2024.3476318

I. INTRODUCTION

PERMANENT magnet synchronous motors (PMSMs) have become increasingly popular in speed control systems, owing to their exceptional power density and efficiency. Compared to field-oriented control, conventional deadbeat predictive current control (DPCC) proves to be a highly effective control method for PMSMs [1], [2]. It exhibits faster dynamic response, superior steady-state performance, and reduced computational complexity. However, the effectiveness of DPCC is significantly reliant on the precision of the PMSM model [3]. Under heavy load working conditions, the stator resistance, stator inductance, and permanent magnet flux are time-varying [4]. Both dynamic and steady-state performances of the PMSM control system may deteriorate due to parameter mismatch, external disturbances, and environmental uncertainties. To overcome the impact of parameter mismatch on DPCC and improve its control performance, model-free predictive current control (MFPCC) techniques have been proposed in [5], [6], [7], [8], [9], [10], [11], [12], [13], [14], [15], [16], [17], [18], [19], [20], [21], [22], [23], and [24]. The MFPCC methods use adaptive models whose parameters are obtained from the collected data. Without the need for motor parameters, the MFPCC demonstrates enhanced performance and robustness in the face of varying working conditions and parameter mismatch.

There are usually two types of MFPCC. The first category involves the storage of current variations [5], [6], [7] instead of conventional PMSM model. This method stores the data of the current measurement variations caused by different voltage vectors in a look-up table (LUT) [5]. Then the predictive current variations are calculated using the stored data. This method assumes that the current gradient remains constant during the adjacent updates of the LUT. Thus, the performance deteriorated under low updating rate of the LUT. Rui et al. [6] proposed a double-vector MFPCC method to eliminate the stagnation phenomenon of the LUT and reduce the current ripple. In [7], the current gradients caused by the applied voltage vectors were estimated using two contiguous measured current gradients, all current gradients can be updated within every control period. In

[8], the conventional control set is extended using discrete space vector modulation.

Instead of the current variations LUT, the second type of MFPCC utilizes an ultralocal model. The mathematical model of PMSM was simplified into a first order system with an unknown term consisted of all the disturbance. To obtain the unknown part of the ultralocal model, several methods have been proposed [9], [10], [11], [12], [13], [14], [15]. In [9], an extended-state observer (ESO) was utilized to obtain the disturbance in the ultra-local model. Zhao et al. [10] simplified the ultra-local model and the disturbance can be directly calculated using the current differences of the past two control periods. Zhou et al. [11] proposed an algebraic parameter identification technique to estimate the optimal angle of the voltage vector. Wei et al. [12] extended the ultralocal model to observe the inertia of the system online, achieving better dynamics and current quality with enhanced robustness. Chen et al. [13] proposed a new ultralocal model considering the motor speed to improve the performance and the robustness. Furthermore, the performance of the ultralocal model was enhanced using the exponential-like error feedback [14], and the nonlinear ESO [15]. However, the simple structure of the ultralocal models cannot reflect the motion characteristics of the motor accurately and timely. In [16], [17], and [18], the data-driven method was used to update the model in the form of discrete-time transfer functions. In [19], a continuous control set data-driven method was developed to achieve better control performance.

Despite that the stator resistance and the permanent magnet flux were not required by using the ultralocal model, the stator inductance was still needed as the control gain. The inductance mismatch caused high-frequency disturbances to the controller and could not be observed due to the limited bandwidth of the ESO [20]. Hence, researchers have focused on developing online methods to estimate inductance [21], [22], [23], [24]. In [21], the stator inductance was obtained using the integral of the d-axis current prediction mismatch. Furthermore, researchers have shown that inductance can be derived by driving the error of the d-axis current prediction to zero using a PI regulator [22], or by employing the gradient descent method [23]. In addition, Wu et al. [24] proposed a new method to directly calculate the inductance parameter, achieving real-time convergence.

Another major disturbance which greatly influences the performance of the MFPCC is the nonlinearity of the inverter [25], [26], [27], [28]. The nonlinearity can be caused by the dead time in the gate signals, finite turn-ON/turn-OFF time, voltage drop, and other unknown physical characteristics of the switching devices [28]. The nonlinearity of the two-level voltage source inverter (2L-VSI) will generate the sixth-order harmonic component in the synchronous frame, which is usually close to or beyond the bandwidth of the ESO [21]. When estimating disturbances using the ESO, significant gain error and phase delay may occur. The estimation error of the disturbance can cause performance distortion of the MFPCC [16], [17], [18]. Conventional MFPCC used offline compensation methods to reduce the disturbance caused by the inverter nonlinearity [22], [24]. Nonetheless, compensating for such nonlinearity precisely

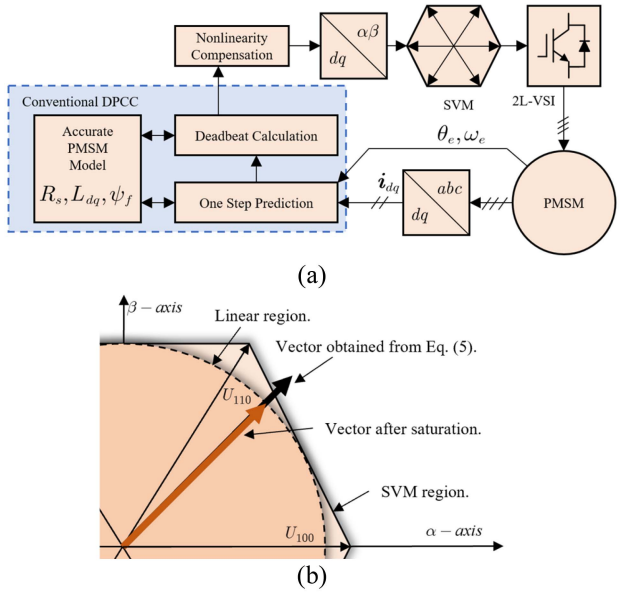

Fig. 1. Control diagram of the conventional DPCC. (a) Overall control diagram. (b) SVM saturation method.

is challenging due to the high number of the time varying parameters required.

Therefore, there is a need to improve the online estimation performance of the ESO specifically for such disturbances. A parallel-cascade ESO was proposed by Jose Rodriguez et al., to enhance the disturbance rejection and noise suppression performance [29], [30], [31]. However, this approach necessitates the parallel and cascade connection of multiple ESO units, leading to additional network configurations and increasing the computational burden. Moreover, the bandwidths and the parameters of all ESO units are pre-set offline, preventing them from sustaining stable performance across full speed range. Xu et al. [32] proposed an improved ESO to observe the disturbance at certain frequency. However, the method was designed to track disturbances that have a much higher frequency than the bandwidth of the ESO. Furthermore, the method still encounters challenges in mitigating gain error and phase delay. In [33], an improved ESO was proposed to eliminate the estimation phase delay in synchronous frequency, but it required the information of stator resistance and additional parameter tuning.

In conclusion, there are three main challenges remaining. First, the disturbance frequency caused by inverter nonlinearity varies with changes in motor speed. Therefore, it is difficult to be tracked adaptively. Second, accurate observation of the disturbance required additional information of the motor and the inverter, etc. Finally, the observer requires complex parameter tuning, and is difficult to be updated adaptively online. To overcome the above challenges, a modified MFPCC (M-MFPCC) with a modified extended state observer (MESO) is proposed in this article. The proposed method achieves three main contributions. To begin with, the proposed MESO enables accurate disturbance observation at full speed range with unit gain and zero phase delay. In this article, the tracking frequency was set

to the 6th harmonic disturbance caused by the inverter nonlinearity. Next, adaptive gain updating for the proposed MESO is achieved with low computation cost to effectively sustain the noise suppression performance while tracking the disturbance when the motor speed varies. Finally, this method requires no additional motor or inverter information, nor does it need extra parameter tuning compared to conventional MFPCC methods. The proposed M-MFPCC has been experimentally verified to exhibit better performance compared to the conventional MFPCC (C-MFPCC) in terms of torque ripple, steady-state torque tracking error, current THD, and parameter robustness.

The rest of this article is organized as follows. Section II provides an overview of the conventional DPCC and the ESO-Based MFPCC. The analysis of the disturbance caused by inverter nonlinearity is also carried out. Section III introduces the proposed M-MFPCC, including the principle of the MESO, the bode diagram analysis, and the control flowchart. Section IV provides the experimental results of the proposed method and other conventional methods to validate the effectiveness, steady-state performance, and parameter robustness. Finally, Section V concludes this article.

II. Conventional ESO-Based MFPCC

A. PMSM Modeling and Conventional DPCC

Neglecting the nonlinearity of the inverter, the dynamics of PMSM in the synchronous dq-axes frame are described as

$$\frac{d}{dt}\boldsymbol{i}_{dq} = \mathbf{A}\boldsymbol{i}_{dq} + \mathbf{B}\boldsymbol{u}_{dq} + \mathbf{D} \tag{1}$$

where

$$\mathbf{A} = \begin{bmatrix} -R_s/L_d & \omega_e L_q/L_d \\ -\omega_e L_d/L_q & -R_s/L_q \end{bmatrix}$$

$$\mathbf{B} = \begin{bmatrix} 1/L_d & 0 \\ 0 & 1/L_q \end{bmatrix}, \mathbf{D} = \begin{bmatrix} 0 \\ -\omega_e \psi_f/L_q \end{bmatrix}$$

are the system matrixes, $\boldsymbol{u}_{dq} = \begin{bmatrix} u_d & u_q \end{bmatrix}^T$ and $\boldsymbol{i}_{dq} = \begin{bmatrix} i_d & i_q \end{bmatrix}^T$ are the dq-axes voltage and current, respectively. $L_d, L_q$are the dq-axes inductances, R_s is the stator resistance, ψ_f is the permanent magnet flux, and ω_e is the rotor electrical speed. The torque of PMSM can be calculated using

$$T_e = \frac{3}{2} P_n \left(\psi_f i_q + \left(L_d - L_q\right) i_d i_q\right) \tag{2}$$

where P_n is the motor poles number. In order to implement the conventional DPCC method based on the accurate model, the discrete model of PMSM can be obtained from (1) as

$$\boldsymbol{i}_{dq}\left(k+1\right) = \left(\mathbf{I} + T_s\mathbf{A}\right)\boldsymbol{i}_{dq}\left(k\right) + T_s\mathbf{B}\boldsymbol{u}_{dq}\left(k\right) + T_s\mathbf{D} \tag{3}$$

where T_s is the control period and $\mathbf{I}$ is the unit matrix. k is the number of the sampling period. Due to the update delay caused by the microcontrollers such as digital signal processors, one-step delay compensation should be introduced from (3) as

$$\hat{\boldsymbol{i}}_{dq}\left(k+1\right) = \left(\mathbf{I} + T_s\mathbf{A}\right)\boldsymbol{i}_{dq}\left(k\right) + T_s\mathbf{B}\boldsymbol{u}_{dq}\left(k\right) + T_s\mathbf{D} \tag{4}$$

where $\hat{\boldsymbol{i}}_{dq}(k+1)$ is the estimation of the current in the $(k+1)^{th}$ control period using the conventional PMSM model. $\boldsymbol{i}_{dq}(k), \boldsymbol{u}_{dq}(k)$ are the dq-axis current and voltage in the k^{th} sampling period, respectively.

Then reference voltage vector of conventional DPCC method $\boldsymbol{u}_{dq}(k+1)$ can be calculated as [16]

$$\boldsymbol{u}_{dq}\left(k+1\right) = T_s^{-1}\mathbf{B}^{-1}\left(\boldsymbol{i}_{dq}^{*} - \left(\mathbf{I} + T_s\mathbf{A}\right)\hat{\boldsymbol{i}}_{dq}\left(k+1\right) - T_s\mathbf{D}\right) \tag{5}$$

where $\boldsymbol{i}_{dq}^{*}$ is the reference current and $\boldsymbol{u}_{dq}(k+1)$ is the required dq-axes voltage vector. Space vector modulation (SVM) technique is used to generate the required voltage vector. The overall control diagram of conventional DPCC is shown in Fig. 1(a). The tracking error of the current is eliminated in the $(k+2)^{th}$ control period if the model (4) is accurate. When the vector exceeds the linear region of the modulation [35], the amplitude of the vector should be saturated to the linear modulation region, as shown in Fig. 1(b). To achieve better performance, inverter nonlinearity compensation is needed [25], [26], [27], [28]. The compensation method will be further introduced in Section IV.

B. Conventional ESO-Based MFPCC

The above conventional DPCC method is highly dependent on the accurate model of the PMSM, which requires the information of R_s, L_{dq} and ψ_f, as shown in Fig. 1 [17], [18], [19]. The parameter mismatch will cause current tracking error and deteriorate the dynamic performance [19]. Therefore, the conventional ESO-based MFPCC (C-MFPCC) is introduced. The ultra-local model can be expressed in the synchronous dq-axes frame as [9]

$$\frac{d}{dt}i_x = \hat{b}_x u_x + f_x, x \in \{d, q\} \tag{6}$$

where $\hat{b}_x = 1/\hat{L}_x$ is the control gain of the dq-axes voltage. $\hat{L}_x$is the estimate inductance used in the model. $x \in \{d, q\}$ is the dq-axis index. f_x is the total disturbance, which can be written as

$$f_d = \left(\frac{1}{L_d} - \frac{1}{\hat{L}_d}\right)u_d + \frac{\omega_e L_q i_q - R_s i_d}{L_d} + f_d'$$

$$f_q = \left(\frac{1}{L_q} - \frac{1}{\hat{L}_q}\right)u_q + \frac{-\omega_e\left(L_d i_d + \psi_f\right) - R_s i_q}{L_q} + f_q' \tag{7}$$

where $f_x', x \in \{d, q\}$ is the un-modeled disturbance, *e.g.*, the disturbance caused by the inverter nonlinearity and the current measurement noise [29], [30], [31]. One can get from (7) that the first term of f_x is caused by the inductance mismatch and will introduce high frequency component into the total disturbance.

The structure of ESO can be constructed as

$$\frac{d}{dt}\hat{i}_x = \hat{b}_x u_x + \hat{f}_x + \beta_1\left(i_x - \hat{i}_x\right)$$

$$\frac{d}{dt}\hat{f}_x = \beta_2\left(i_x - \hat{i}_x\right) \tag{8}$$

where $\hat{i}_x$ and $\hat{f}_x$ are the current estimation and the total disturbance estimation using the ESO, respectively. $\beta_y, y \in \{1, 2\}$ is the gain of the ESO. Unlike the Luenberger observer (LO), the ESO extracts disturbances within the model as a virtual state variable and observes it, thereby enhancing the traditional

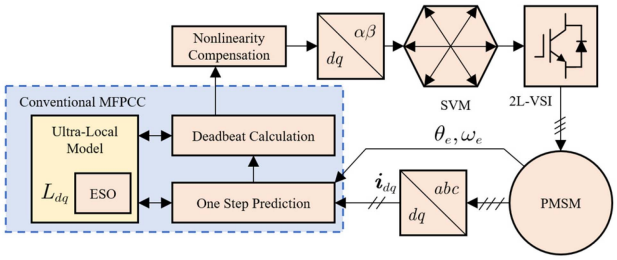

Fig. 2. Control diagram of the C-MFPCC.

LO's capability in disturbance observation. In order to analyze the frequency domain performance of the ESO in (8), Laplace transform is performed to (6) and (8) as

$$\begin{aligned} sI_x &= \hat{b}_x U_x + F_x \\ s\hat{I}_x &= \hat{b}_x U_x + \hat{F}_x + \beta_1 \left(I_x - \hat{I}_x\right) \\ s\hat{F}_x &= \beta_2 \left(I_x - \hat{I}_x\right). \end{aligned} \tag{9}$$

One can get the transfer function of the total disturbance estimation from (9) as [29]

$$G_{ff}(s) = \frac{\hat{F}_x}{F_x} = \frac{\beta_2}{s^2 + s\beta_1 + \beta_2} \tag{10}$$

where $G_{ff}(s)$ is the transfer function of the total disturbance estimation. In order to get stability and better dynamic performance, the two roots of (10) are set to ω_b, which is the bandwidth of the ESO [9]

$$\beta_1 = 2\omega_b, \beta_2 = {\omega_b}^2. \tag{11}$$

The choice of bandwidth for the ESO is a critical factor in achieving fast convergence and efficient noise suppression. In scholarly literature, it is common practice to set the bandwidth around 10 p.u., considering the rated electrical frequency of the motor as the reference value [22], [24]. The control diagram of the C-MFPCC is shown in Fig. 2.

The ESO shown in (8) is discretized as

$$\begin{aligned} \hat{i}_x(k+1) &= \hat{i}_x(k) + T_s \begin{pmatrix} \hat{b}_x u_x(k) + \hat{f}_x(k) \\ +\beta_1 \left(i_x(k) - \hat{i}_x(k)\right) \end{pmatrix} \\ \hat{f}_x(k+1) &= \hat{f}_x(k) + T_s \beta_2 \left(i_x(k) - \hat{i}_x(k)\right). \end{aligned} \tag{12}$$

Compared to the estimation of the conventional DPCC based on the accurate model in (4), the ESO based ultra-local model only requires the information of the stator inductance, as shown in Fig. 2. Thus, the robustness of the model is enhanced [10]. After the one-step delay compensation, one can get the reference voltage vector using the same deadbeat principle in (5) as

$$u_x(k+1) = {T_s}^{-1} \hat{b}_x^{-1} \left(i_x^* - \hat{i}_x(k+1) - T_s \hat{f}_x(k+1)\right). \tag{13}$$

Finally, to achieve superior performance, it is crucial to include inverter nonlinearity compensation in the control scheme to compensate the un-modeled term f_x' in (6), which will be discussed in Section II-C.

C. Disturbance Analysis Considering 2L-VSI Nonlinearity

Among the unmodeled disturbance described in (7), the nonlinearity and the unsymmetric output voltage of the 2L-VSI constitute one of the most severe disturbances. Therefore, this article primarily focuses on addressing and mitigating this particular type of disturbance. Ignoring the turn-ON/turn-OFF dynamics of the switching components, the disturbance caused by the 2L-VSI can be structured theoretically as [28]

$$v_z = v_{\text{err}} \text{sign}(i_z), z \in \{a, b, c\} \tag{14}$$

where v_z is the error voltage between the reference phase voltage and the real phase voltage output, v_{err} is the theoretical amplitude of the disturbance, i_z is the phase current, $\text{sign}(\cdot)$ is a signum function, $z \in \{a, b, c\}$ is the index of the three half-bridges of the 2L-VSI and

$$v_{\text{err}} = \frac{T_{\text{dead}} + T_{\text{on}} - T_{\text{off}}}{T_s} (v_{\text{dc}} - v_{ce} + v_d) + \frac{v_{ce} + v_d}{2} \tag{15}$$

where T_{dead} is the dead time, $T_{\text{on}}, T_{\text{off}}$ are the turn-ON and turn-OFF time of the switching component, respectively. $v_{\text{dc}}$is the dc bus voltage. v_{ce} and v_d are the voltage drops of the switching component and the freewheeling diode, respectively. It is important to note that all parameters of the 2L-VSI discussed above are variable and subject to change based on the half-bridge current, except the dead time.

Assuming that the motor ran at $i_d = 0$ control strategy and the rotor position is $\theta_e = \omega_e t$. One can take the a phase current in the motor windings as an example

$$i_a = I_c \sin(\omega_e t + \pi) \tag{16}$$

where I_c is the amplitude of the phase current. The phase currents of the other two windings are $2/3\pi$ and $4/3\pi$ delayed, respectively.

Substituting (16) into (14), one can get the Fourier expansion form as

$$\begin{cases} v_a = v_{err} \frac{4}{\pi} \sum \frac{\sin(n(\omega_e t + \pi))}{n} \\ v_b = v_{err} \frac{4}{\pi} \sum \frac{\sin\left(n\left(\omega_e t + \pi - 2/3\pi\right)\right)}{n} \\ v_c = v_{err} \frac{4}{\pi} \sum \frac{\sin\left(n\left(\omega_e t + \pi - 4/3\pi\right)\right)}{n} \end{cases}, n \in \{1, 3, 5, \ldots\}. \tag{17}$$

One can get from (17) that the $3k$th order harmonic disturbances in the three-phase system act as common mode components [34]. Therefore, only the remaining harmonics of $6k-1\text{th}, 6k+1\text{th}$ exist in the phase current. One can get the disturbance in the dq-axes synchronous frame as

$$\begin{cases} v_d = -\frac{4v_{\text{err}}}{\pi} \sum \frac{\sin(n\omega_e t)}{n} \\ v_q = \frac{4v_{\text{err}}}{\pi} - \frac{4v_{\text{err}}}{\pi} \sum \frac{\cos(n\omega_e t)}{n} \end{cases}, n \in \{6, 12, \ldots\}. \tag{18}$$

Equation (18) indicates that the disturbance caused by the inverter nonlinearity introduces dc biases and $6k$th harmonics to the dq frame. As discussed in Section II-B, the bandwidth of the ESO is usually set to around 10 p.u. When the motor ran at rated speed, the frequency of the 6th harmonic is close to the ESO bandwidth, while the $12\text{th}, 18\text{th}, \ldots$ harmonics are beyond the bandwidth. Therefore, the disturbance tracking performance of

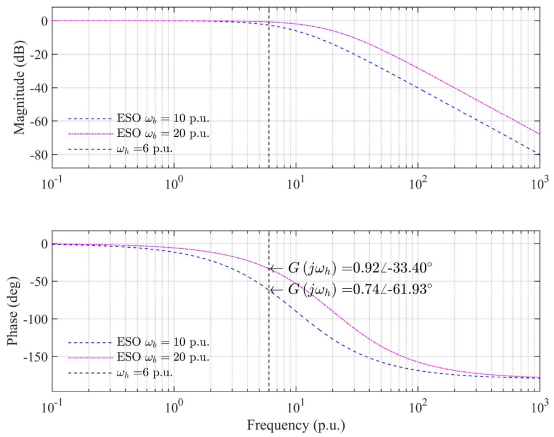

Fig. 3. Bode diagram of conventional ESO under different bandwidths.

the ESO deteriorates when faced with the disturbance caused by inverter nonlinearity due to limited bandwidth.

The bode diagram of (10) under different bandwidths are shown in Fig. 3., where ω_h is the frequency of the sixth harmonic disturbance, i.e., 6 p.u when the motor is at rated speed. For bandwidth of 10 p.u., the gain of the transfer function is 0.74 and the phase delay is 61.93°. It suggests that estimating sixth harmonic disturbances by conventional ESO may suffer from significant gain error and phase delay.

In addition, the bode diagram of conventional ESO under 20 p.u. bandwidth is also shown in Fig. 3. Increasing the bandwidth ensures improved estimation performance. However, this comes at the cost of degraded noise suppression capabilities, and the limited in phase delay is slight.

III. Proposed Modified MFPCC

A. Design of the Proposed MESO

Considering the disturbance at certain frequency ω_h as

$$h = A_h \sin\left(\omega_h t + \phi_h\right) \tag{19}$$

where h is the certain frequency disturbance, A_h is the amplitude and ϕ_h is the phase of the disturbance. One can get the dynamics of (19) as

$$\frac{d^2}{dt^2}h = -{\omega_h}^2 A_h \sin\left(\omega_h t + \phi_h\right) = -{\omega_h}^2 h. \tag{20}$$

This illustrates the proportionality between the second derivative of a disturbance and the disturbance itself. Thus, disturbance in (7) can be reconstructed as

$$\begin{aligned} \frac{d}{dt}i_x &= \hat{b}_x u_x + f_x + h_x \\ \frac{d^2}{dt^2}h_x &= -{\omega_h}^2 h_x \end{aligned} \tag{21}$$

where $h_x, x \in \{d, q\}$ is the disturbance under frequency ω_h in the dq-axes. Thus, the proposed MESO is constructed as

$$\begin{aligned} \frac{d}{dt}\hat{i}_x &= \hat{b}_x u_x + \hat{f}_x + \hat{h}_x + \beta_1\left(i_x - \hat{i}_x\right) \\ \frac{d}{dt}\hat{f}_x &= \beta_2\left(i_x - \hat{i}_x\right) \\ \frac{d}{dt}\hat{h}_x &= \hat{d}_x + \beta_3\left(i_x - \hat{i}_x\right) \\ \frac{d}{dt}\hat{d}_x &= -{\omega_h}^2\hat{h}_x + \beta_4\left(i_x - \hat{i}_x\right) \end{aligned} \tag{22}$$

where $d_x = \frac{d}{dt}h_x$ is the first derivative and $\beta_y, y \in \{1, \ldots, 4\}$ are the gain of the MESO. $y \in \{1, \ldots, 4\}$ is the index of the observer gain. To guarantee the same stability and noise suppression performance as the conventional ESO, the four roots of the observer are all set to ω_b, which leads to

$$\begin{aligned} \beta_1 &= 4\omega_b \\ \beta_2 &= {\omega_b}^4/{\omega_h}^2 \\ \beta_3 &= -\left({\omega_b}^4 - 6{\omega_b}^2{\omega_h}^2 + {\omega_h}^4\right)/{\omega_h}^2 \\ \beta_4 &= 4{\omega_b}^3 - 4\omega_b{\omega_h}^2. \end{aligned} \tag{23}$$

In order to analyze the frequency domain performance of the MESO in (22), Laplace transform is performed to (22) and (21) as

$$\begin{aligned} sI_x &= \hat{b}_x U_x + F_x + H_x \\ s\hat{I}_x &= \hat{b}_x U_x + \hat{F}_x + \hat{H}_x + \beta_1\left(I_x - \hat{I}_x\right) \\ s\hat{F}_x &= \beta_2\left(I_x - \hat{I}_x\right) \\ s\hat{H}_x &= \hat{D}_x + \beta_3\left(I_x - \hat{I}_x\right) \\ s\hat{D}_x &= -{\omega_h}^2\hat{H}_x + \beta_4\left(I_x - \hat{I}_x\right). \end{aligned} \tag{24}$$

The transfer function of the estimated total disturbance can be obtained from (24) as

$$\begin{aligned} G_{ff}(s) &= \frac{\hat{F}_x + \hat{H}_x}{F_x + H_x} \\ &= \frac{s^2\left(6{\omega_b}^2 - {\omega_h}^2\right) + 4s\left({\omega_b}^3 - \omega_b{\omega_h}^2\right) + {\omega_b}^4}{\left(s + \omega_b\right)^4}. \end{aligned} \tag{25}$$

From (25), it can be observed that the transfer function of the disturbance estimation is augmented with two extra zeros and poles. In addition, the gain and the phase of the transfer function under ω_h can be deduced from (25) as

$$G_{ff}(j\omega_h) = 1\angle 0°. \tag{26}$$

Equation (26) suggests that accurate estimation of the disturbance at particular frequency ω_h can be achieved with unity gain and no phase delay. Therefore, by setting the frequency to $\omega_h = 6\omega_e$, ω_e representing the motor real time electrical frequency, the proposed MESO can precisely track the sixth harmonic disturbance injected by the inverter nonlinearity.

The bode diagram of the proposed MESO is shown in Fig. 4. When the motor ran at rated speed, i.e., the frequency of the $6kth$ harmonic disturbance by inverter nonlinearity is 6 p.u., the gain and phase delay of the estimation transfer function (26)

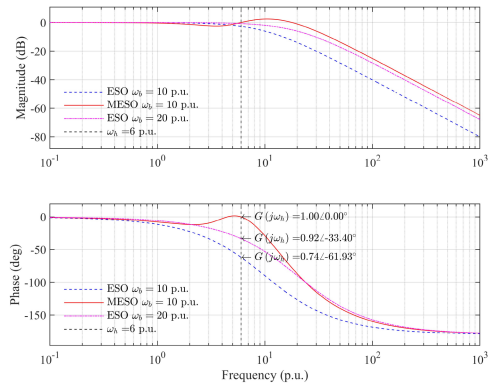

Fig. 4. Bode diagram of the proposed MESO. Motor runs at rated speed. Disturbance frequency is 6 p.u.

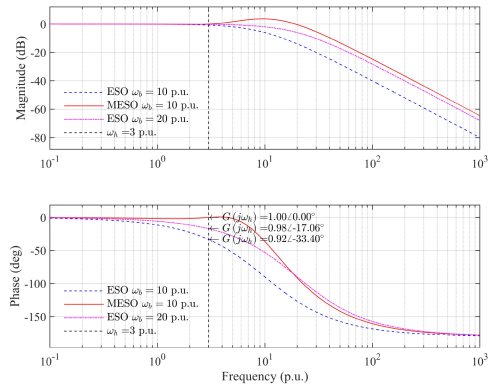

Fig. 5. Bode diagram of the proposed MESO. Motor runs at 0.5 p.u. speed. Disturbance frequency is 3 p.u.

under 10 p.u. bandwidth is shown. The figure illustrates that the MESO provides precise estimation with unity gain and no phase delay. Consequently, the estimation performance of the MESO is enhanced compared to the conventional ESO.

When the motor speed varies, ω_h and the observer gain in (22) can be updated in real time. Fig. 5 shows the disturbance estimation of the proposed MESO and conventional ESOs when the motor ran at 0.5 p.u. speed. For conventional ESOs, when compared with Fig. 4, the estimation gain error decreases because the frequency of the disturbance drops from 6 p.u. to 3 p.u. However, the phase delay still maintained to be 33.4° for 10 p.u. bandwidth and 17.06° for 20 p.u. bandwidth. For the proposed MESO, unity gain and no phase delay still hold due to the real-time update of the observer coefficients. In both Figs. 4 and 5, overshoots are observed around the bandwidth ω_b for MESO.

However, since the disturbance component at this frequency is insignificant, these overshoots are not expected to notably affect the performance of the MESO.

B. Proposed M-MFPCC

The control diagram of the proposed M-MFPCC is shown in Fig. 6. First, the MESO is discretized as

$$\hat{i}_x(k+1) - \hat{i}_x(k) = T_s \begin{pmatrix} \hat{b}_x u_x(k) + \hat{f}_x(k) + \hat{h}_x(k) \\ +\beta_1(k)\left(i_x(k) - \hat{i}_x(k)\right) \end{pmatrix}$$

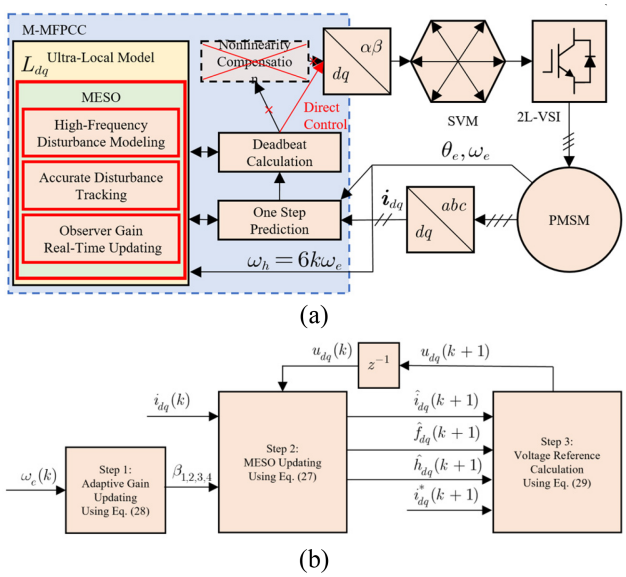

Fig. 6. Control diagram of the proposed M-MFPCC. (a) Overall control diagram. (b) Detailed flowchart of the proposed method.

$$\begin{aligned} \hat{f}_x(k+1) - \hat{f}_x(k) &= T_s \beta_2(k)\left(i_x(k) - \hat{i}_x(k)\right) \\ \hat{h}_x(k+1) - \hat{h}_x(k) &= T_s\left(\hat{d}_x(k) + \beta_3(k)\left(i_x(k) - \hat{i}_x(k)\right)\right) \\ \hat{d}_x(k+1) - \hat{d}_x(k) &= T_s \begin{pmatrix} -{\omega_h}^2 \hat{h}_x(k) \\ +\beta_4(k)\left(i_x(k) - \hat{i}_x(k)\right) \end{pmatrix}. \end{aligned} \tag{27}$$

The observer gain $\beta_y(k), y \in \{1, \ldots, 4\}$is updated by substituting real-time motor speed into (23) as

$$\begin{aligned} \beta_1(k) &= 4\omega_b \\ \beta_2(k) &= {\omega_b}^4 \Big/ \omega_h(k)^2 \\ \beta_3(k) &= -\left({\omega_b}^4 - 6{\omega_b}^2 \omega_h(k)^2 + \omega_h(k)^4\right) \Big/ \omega_h(k)^2 \\ \beta_4(k) &= 4{\omega_b}^3 - 4\omega_b \omega_h(k)^2 \end{aligned} \tag{28}$$

where $\omega_h(k) = 6\omega_e(k)$ is the frequency of the sixth harmonic disturbance injected by the inverter nonlinearity in the kth sampling period. Then, the reference voltage vector of the M-MFPCC can be obtained using the deadbeat principle in (5) as

$$u_x(k+1) = {T_s}^{-1} \hat{b}_x^{-1} \begin{pmatrix} i_x^* - \hat{i}_x(k+1) \\ -T_s \hat{f}_x(k+1) - T_s \hat{h}_x(k+1) \end{pmatrix}. \tag{29}$$

With improved disturbance rejection against inverter nonlinearity, M-MFPCC can directly control the voltage vector without additional requirement of motor or the inverter to compensate the output voltage.

IV. Experimental Results

To demonstrate the effectiveness of the proposed approach, a comparative analysis is conducted between the M-MFPCC

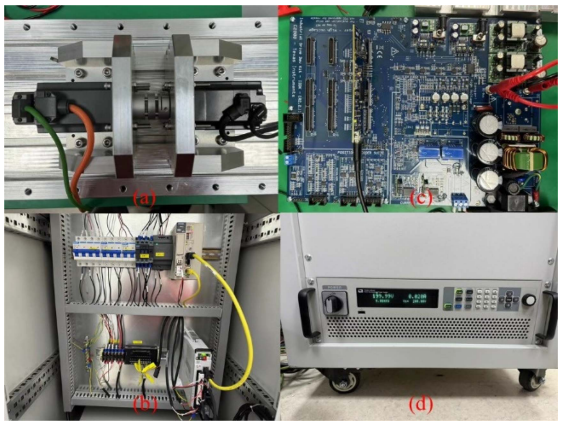

Fig. 7. Experimental platform. (a) Test motor and load motor. (b) Control system of the load motor. (c) Inverter of the test motor. (d) DC power supply.

TABLE I
PARAMETERS OF THE TESTED PLATFORM

	Parameter	Value
PMSM	Poles	8
	Stator Resistance	3.2 Ω
	Stator Inductance	5.97 mH
	Permanent-Magnet Flux Linkage	0.055 Wb
	Rated Speed	1000 r/min
	Rated Current	3.6 A (Peak)
	Rated Torque	1.27 Nm
Inverter	DC Bus Voltage	300 V
	Switching Frequency	16 kHz
	IPM Model	PS21765
	Collector-Emitter Saturation Voltage	1.6V @30A
	Diode Forward Voltage	1.5V@30A
	Turn-ON Time	1.3 us @30A
	Turn-OFF Time	1.5 us @30A
Controller	Bandwidth of ESO	10 p.u.
	Dead Time	2.0 us

and two other methods: the conventional DPCC equipped with inverter nonlinearity compensation (DPCC-NC), and the C-MFPCC. The bandwidths of both the C-MFPCC and the proposed M-MFPCC are set to 10 p.u. Steady-state experiments of the above three methods are carried out using the PMSM platform shown in Fig. 7. Table I gives the parameters of the test motor and the inverter. The performance of the three methods under inductance parameter mismatch were also tested.

To guarantee the computation performance in (28), careful selection of the minimum value of ω_h is crucial. When motor ran at very low speed, ω_h is significantly smaller than ω_b, the total transfer function of the MESO (25) can be simplified to

$$G_{ff} = \frac{6{\omega_b}^2 s^2 + 4s{\omega_b}^3 + {\omega_b}^4}{(s+\omega_b)^4} \tag{30}$$

which indicates that the update of very low ω_h will not effectively influence the performance of the MESO. Therefore, after experimental verifications, the general minimum value was set to

$$\omega_{h,\min} = 0.01\omega_b. \tag{31}$$

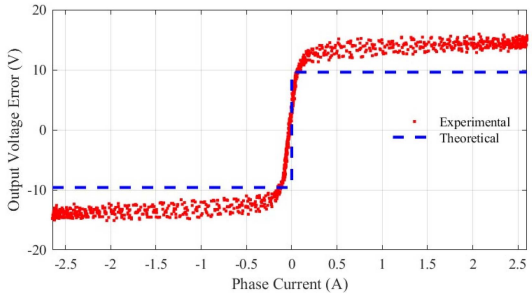

Fig. 8. Output phase voltage error of the tested inverter.

By substituting $\omega_b = 10(\text{p.u.})$ into (31), one can get $\omega_{h,\min} = 0.1(\text{p.u.})$.

To validate the accurate nonlinearity disturbance of the tested inverter, the output error voltage was measured experimentally offline when the motor stopped. First, a reference dc voltage u^*_{ab} was added to the A and B phase of the motor, leaving the C phase open-circuit. One can get the voltage equations of the A and B phase as

$$u^*_{ab} = v_a(i_a) + R_s i_a - v_b(i_b) - R_s i_b. \tag{32}$$

Assuming that the three phase of the inverter was symmetrical, and $\sum_{z=a,b,c} i_z = 0$,one can get from (32) that

$$u^*_{ab} = 2v(i) + 2R_s i \tag{33}$$

where

$$v(i) = v_z(i), z \in \{a,b,c\}$$
$$i = i_a = -i_b. \tag{34}$$

Therefore, one can get the experimental data of inverter nonlinearity error from (33) as

$$v(i) = \frac{1}{2}u^*_{ab} - R_s i. \tag{35}$$

The experimental data collected using (35) and the theoretical value calculated using (15) are shown in Fig. 8. It indicates that the theatrical value cannot reflect the characteristics of the inverter accurately. Therefore, the DPCC-NC used the experimental data to compensate for the inverter nonlinearity as

$${u_z}^{**} = {u_z}^* + v(i_z) \tag{36}$$

where ${u_z}^{**}$ is the reference voltage value after the compensation. It should be highlighted that the compensation method used in the DPCC-NC required offline data collection, large memory storage and increased computation burden. Therefore, the experimental results of DPCC-NC serve only as a reference under ideal nonlinearity compensation condition. The computation durations of the three methods are 13.6 us for C-MFPCC, 14.2 us for M-MFPCC and 14.7 us for DPCC-NC.

A. Steady-State Performance

To verify the effectiveness and feasibility of the proposed method, simulations were conducted using MATLAB and Simulink. The simulation results of C-MFPCC and M-MFPCC

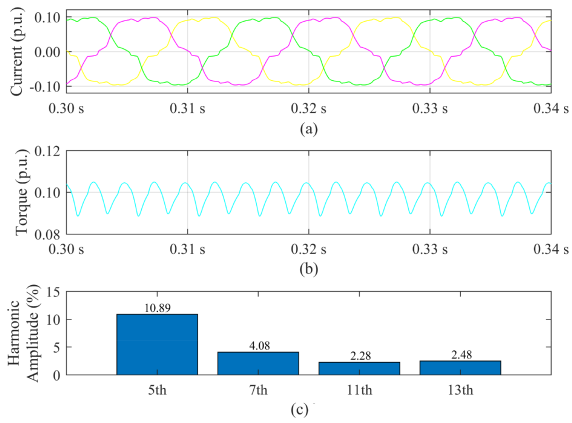

Fig. 9. Simulation results of the C-MFPCC under rated speed and 0.1 p.u. load. (a) Time (s). (b) and (c) Harmonic order.

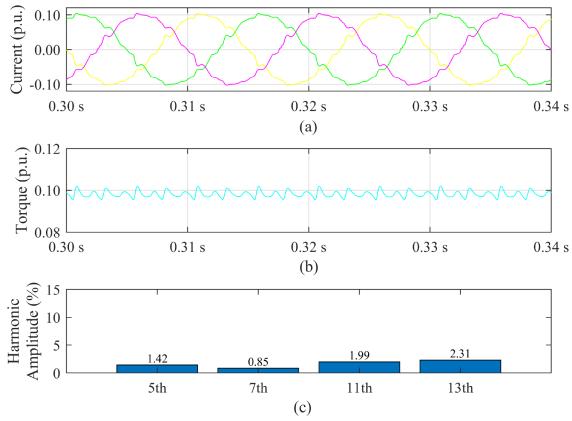

Fig. 10. Simulation results of the M-MFPCC under rated speed and 0.1 p.u. load. (a) Time (s). (b) and (c) Harmonic order.

are shown in Figs. 9 and 10, respectively. The motor operated at rated speed with a 0.1 p.u. load. Figs. 9(a) and 10(a) show the three-phase current waveforms for both methods. The M-MFPCC achieves a more sinusoidal current waveform compared to the C-MFPCC. Torque waveforms are presented in Figs. 9(b) and 10(b), where the M-MFPCC effectively reduces torque ripple from 1.6% p.u. to 0.7% p.u. Harmonic components of both methods are illustrated in Figs. 9(c) and 10(c), revealing that the fifth and seventh harmonics of M-MFPCC are lower than those of C-MFPCC. In conclusion, simulation results indicate that M-MFPCC successfully reduces current harmonics and torque ripple compared to C-MFPCC.

Then, comparative experiments between M-MFCC. C-MFPCC and DPCC-NC were conducted. Fig. 11 showed the steady-state performance of the three methods when the motor operated under rated speed and 0.1 p.u. load. The yellow, purple and green traces in the figures are the three phase currents of the motor. The blue trace is the instant torque control error of the motor. Both the torque ripple and the steady-state torque tracking error can be obtained from the blue trace. The DPCC-NC method achieved minimum torque ripple and current distortion among all methods, which is 1.03%. This is due to the overall offline inverter nonlinearity compensation and accurate PMSM model.

TABLE II
THD RATIOS OF THE TESTED METHODS

Speed (p.u.)	Torque (p.u.)	Method	THD (%)
1.0	0.1	C-MFPCC	7.77
		M-MFPCC	3.49
		DPCC-NC	2.06
1.0	1.0	C-MFPCC	2.68
		M-MFPCC	1.02
		DPCC-NC	0.48
0.5	0.5	C-MFPCC	2.99
		M-MFPCC	0.88
		DPCC-NC	0.68

For the C-MFPCC, the torque ripple is 1.89%, which is larger than the DPCC-NC. This is because that in rated speed, the inverter nonlinearity leads to high frequency voltage error disturbances. The observation of conventional ESO to these disturbances causes gain error and phase delay due to the limited bandwidth of the ESO.

The M-MFPCC exhibits a torque ripple of 1.24%, which is 34.4% lower than that of the C-MFPC. This improvement is attributed to the innovative MESO structure employed in the M-MFPCC. The MESO effectively mitigates observation errors related to the sixth harmonic induced by inverter nonlinearity, thereby enhancing torque quality and reducing current distortion. Consequently, the M-MFPCC achieves lower torque ripple compared to the C-MFPCC, while also demonstrating superior torque tracking accuracy compared to the DPCC-NC.

To further validate the performance of the proposed method, the current and torque waveforms under rated conditions are also tested, as shown in Fig. 12. When using the proposed M-MFPCC, the torque ripple reduced 47.0% when compared with the C-MFPCC. Furthermore, the tracking error of the M-MFPCC is lower than the DPCC-NC. In addition, the DPCC-NC has larger steady-state torque error. This is due to the parameter mismatches between the model used in the DPCC-NC and the real platform. These mismatches are usually caused by unknown disturbances, e.g., the saturation effect of the motor core.

To validate the harmonic rejection ability of the proposed method, the FFT results of the current waveforms are illustrated in Fig. 13. Under 0.1 p.u. load condition, the proposed M-MFPCC reduced the fifth and seventh harmonics to 0.64% and 0.35%, respectively, compared to 7.12% and 1.76% for the C-MFPCC. Furthermore, the performance of the M-MFPCC is superior to that of the ideal DPCC-NC in terms of the fifth and seventh harmonics. For the 11th and 13th harmonics, the M-MFPCC is slightly lower than the C-MFPCC and maintains the same level as the DPCC-NC. In rated load conditions, the proposed M-MFPCC still maintained the lowest level in terms of the fifth and seventh harmonic among the three methods, which are 0.15% and 0.08%. For the 11th and the 13th harmonics, the ideal DPCC-NC exhibits superior performance compared to the two model-free methods. The proposed M-MFPCC is slightly lower than the C-MFPCC.

The harmonics component ratios and the THDs of the three methods in more working conditions are further illustrated in Table II. Under rated condition, the M-MFPCC reduced the THD ratio to 1.02%, which is 61.9% reduction than the conventional C-MFPCC. For low load and middle load conditions, the THD of

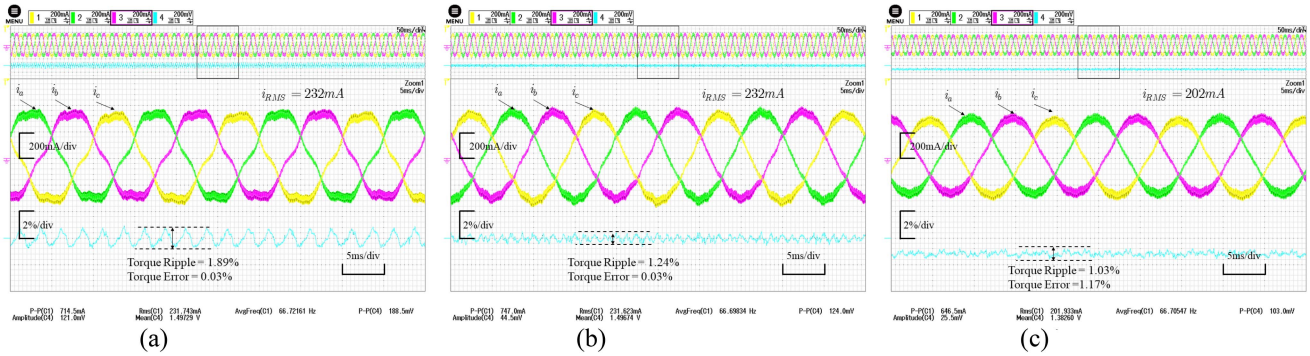

Fig. 11. Current and torque waveforms of the tested methods. Motor ran at rated speed and 0.1 p.u. load. (a) C-MFPCC. (b) M-MFPCC. (c) DPCC-NC.

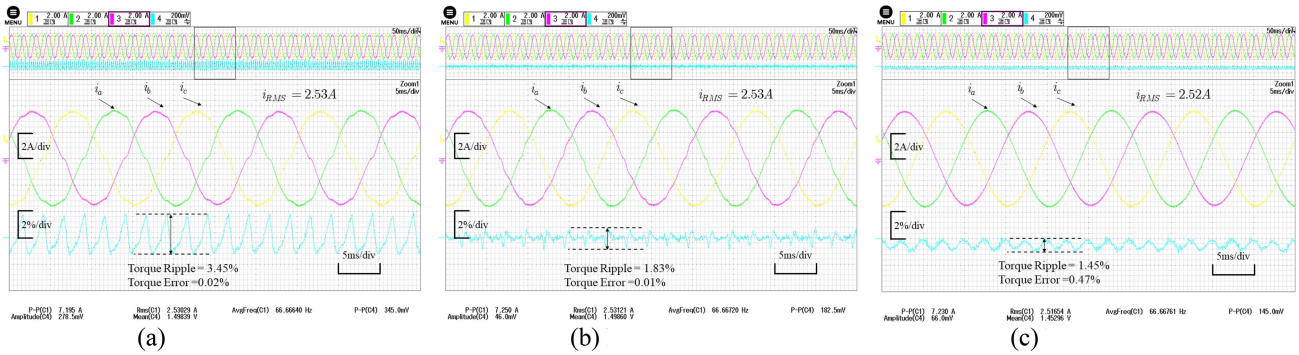

Fig. 12. Current and torque waveforms of the tested methods. Motor ran at rated speed and rated load. (a) C-MFPCC. (b) M-MFPCC. (c) DPCC-NC.

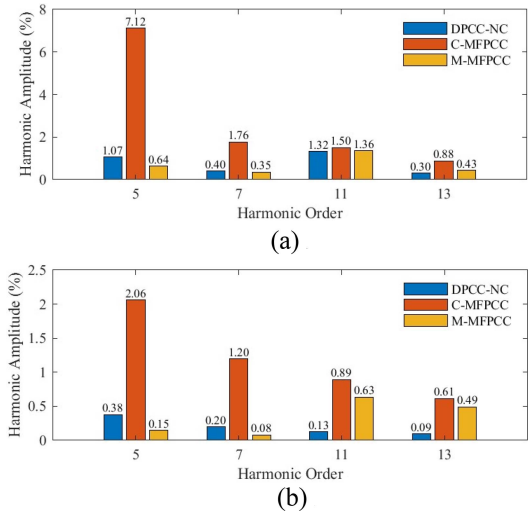

Fig. 13. FFT Analysis of the steady-state current waveforms. (a) Rated speed and 0.1 p.u. load. (b) Rated speed and rated load.

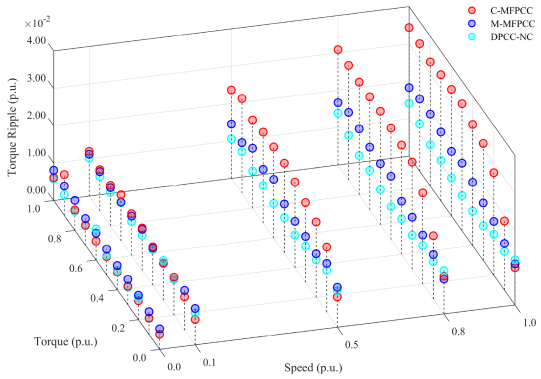

Fig. 14. Torque ripples of the three methods at full speed and load range.

the M-MFPCC is 3.49% and 0.88%, respectively. The reductions compared to the C-MFPCC are 55.1% and 70.5%, respectively. In conclusion, the M-MFPCC proves effective with superior THD performance and lower torque ripple compared to the C-MFPCC in a wide range of operating conditions. Moreover, it exhibits reduced fifth and seventh harmonics in comparison to the DPCC-NC.

To further compare the torque quality among the three methods, torque ripples across the full speed/load range were tested, covering zero speed, low speed (0.1 p.u.), medium speeds (0.5 and 0.8 p.u.), and rated speed. The results are shown in Fig. 14. At zero and low speeds, the performance of the three methods was similar due to the negligible observation errors of M-MFPCC and C-MFPCC at low frequencies. At medium and high speeds, the torque ripple of M-MFPCC is significantly lower than the C-MFPCC. In conclusion, the M-MFPCC can effectively reduce the torque ripple when compared to the C-MFPCC at medium and high speed. All methods have similar torque ripple at zero to low speed.

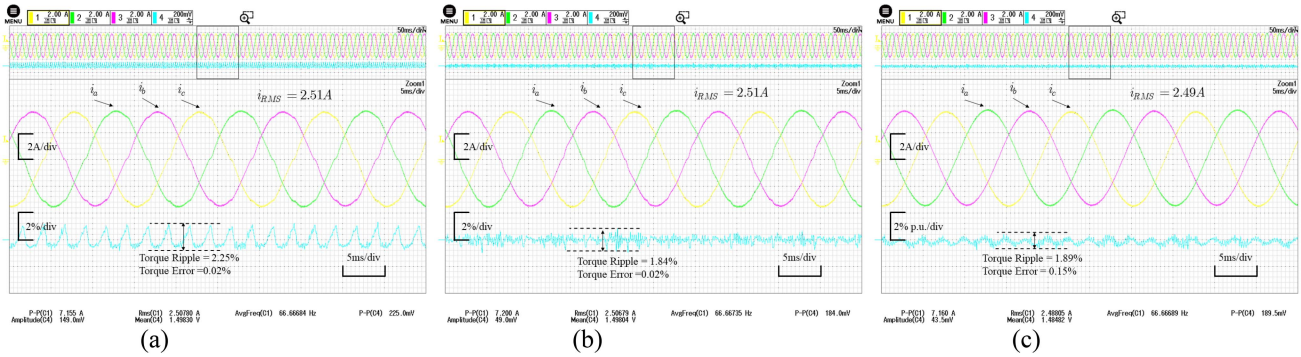

Fig. 15. Current and torque waveforms of the tested methods under 60% inductance mismatch. Motor ran at rated speed and rated load. (a) C-MFPCC. (b) M-MFPCC. (c) DPCC-NC.

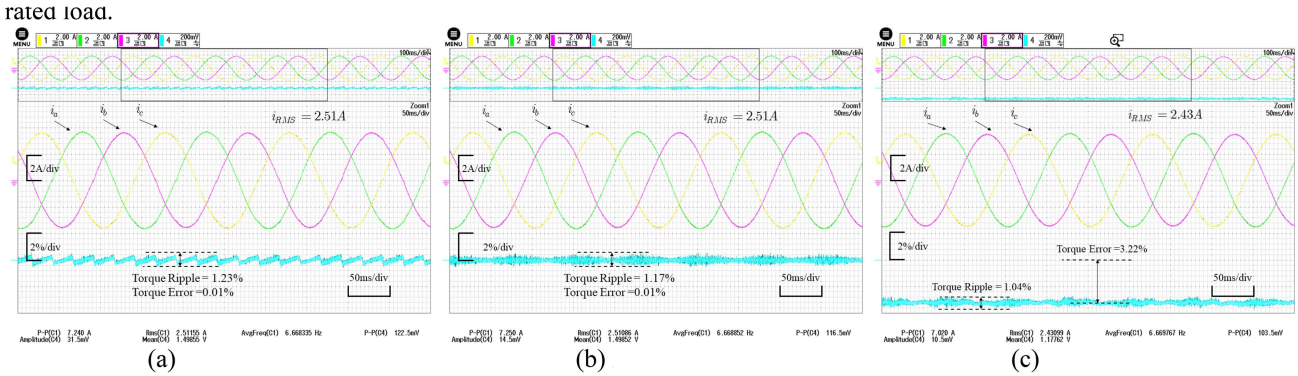

Fig. 16. Current and torque waveforms of the tested methods under 150% resistance mismatch. Motor ran at 0.1 p.u. speed and rated load. (a) C-MFPCC. (b) M-MFPCC. (c) DPCC-NC.

TABLE III
TESTED CONDITIONS IN THE EXPERIMENTS

Tested mismatch conditions		Inductance mismatch	Resistor mismatch
Nominal value of the test rig.		5.97 mH	3.2 Ω
Value used in the controllers		9.95 mH	2.1 Ω
Mismatch rate		$L_{dq}/\hat{L}_{dq} = 60\%$	$R_s/\hat{R}_s = 150\%$
Other parameters		Same as Table I	Same as Table I
Motor operating conditions	Speed	1.0 p.u.	0.1 p.u.
	Torque	1.0 p.u.	1.0 p.u.

B. Parameter Sensitivity

In heavy load conditions, the stator inductance decreases due to core saturation effects, while the stator resistance increases with rising temperature. Therefore, robustness of the three methods to these parameters is crucial. To validate the parameter robustness of the three methods, the steady-state current waveforms under parameter mismatch conditions are tested. The parameter mismatch is simulated by deliberately changing the parameters used in the controllers. The detailed test conditions are given in Table III, where $\hat{L}_{dq}, \hat{R}_s$ are the parameters used in the controllers and L_{dq}, R_s are the nominal value.

First, robustness against decreased inductance is evaluated using configurations detailed in the second column of Table III, where the nominal inductance is 60% of the controllers' parameter. The motor operated at rated speed and torque, and the results are depicted in Fig. 15. Among the methods, M-MFPCC exhibits the least torque ripple at 1.84%. The torque tracking error performances of the three methods are similar. Additionally, all methods exhibit larger high-frequency components in the torque waveforms compared to those with accurate models as shown in Fig. 12, due to inductance mismatch.

Next, robustness against increased resistance is also evaluated, with results presented in Fig. 16. The nominal resistance is 150% of the parameter used in the controllers, as detailed in the third column of Table III. DPCC-NC shows the lowest torque ripple at 1.04%. However, it exhibits a significant torque tracking error of 3.22% due to the pronounced influence of resistance mismatch under low speed and heavy load conditions. In contrast, M-MFPCC demonstrates slightly lower torque ripple compared to C-MFPCC and maintains good torque tracking accuracy.

As a result, both C-MFPCC and M-MFPCC exhibit stronger robustness against resistance mismatch compared to DPCC-NC, attributable to their ultralocal model rather than the conventional

PMSM model. All methods show increased high-frequency torque components in the presence of inductance mismatch. Under both testing conditions, M-MFPCC demonstrates lower torque ripple than C-MFPCC.

V. Conclusion

This article proposed an M-MFPCC method equipped with the proposed MESO which enables accurate disturbance observation at a specific frequency. The proposed method can enhance the disturbance rejection performance against high frequency harmonics caused by the inverter nonlinearity. It achieves better performance than the conventional MFPCC in a wide range of working conditions in terms of torque ripple, steady-state torque tracking error, and current distortion. Furthermore, it showed better performance than the ideal DPCC-NC under heavy load conditions. In addition, the proposed MESO eliminates the requirement of complicated compensation of the inverter nonlinearity and is easy to be implemented to other fields, such as torque ripple rejection. In terms of the parameter mismatch, the proposed M-MFPCC shows better robustness against inductance mismatch than the other tested methods.

References

[1] Y. Wang, S. Fang, and D. Huang, "An improved model-free active disturbance rejection deadbeat predictive current control method of PMSM based on data-driven," *IEEE Trans. Power Electron.*, vol. 38, no. 8, pp. 9606–9616, Aug. 2023.

[2] K. Yu, Z. Wang, W. Hua, and M. Cheng, "Robust cascaded deadbeat predictive control for dual three-phase variable-flux PMSM considering intrinsic delay in speed loop," *IEEE Trans. Ind. Electron.*, vol. 69, no. 12, pp. 12107–12118, Dec. 2022.

[3] X. Zhang, B. Hou, and Y. Mei, "Deadbeat predictive current control of permanent-magnet synchronous motors with stator current and disturbance observer," *IEEE Trans. Power Electron.*, vol. 32, no. 5, pp. 3818–3834, May 2017.

[4] T. Shi, Y. Yan, Z. Zhou, M. Xiao, and C. Xia, "Linear quadratic regulator control for PMSM drive systems using nonlinear disturbance observer," *IEEE Trans. Power Electron.*, vol. 35, no. 5, pp. 5093–5101, May 2020.

[5] C. -K. Lin, T. -H. Liu, J. Yu, L. -C. Fu, and C. -F. Hsiao, "Model-free predictive current control for interior permanent-magnet synchronous motor drives based on current difference detection technique," *IEEE Trans. Ind. Electron.*, vol. 61, no. 2, pp. 667–681, Feb. 2014.

[6] T. Rui et al., "Double-vector model-free predictive current control method for voltage source inverters with sampling noise suppression," *IEEE Trans. Ind. Electron.*, vol. 71, no. 6, pp. 5797–5806, Jun. 2024.

[7] C. Ma, H. Li, X. Yao, Z. Zhang, and F. De Belie, "An improved model-free predictive current control with advanced current gradient updating mechanism," *IEEE Trans. Ind. Electron.*, vol. 68, no. 12, pp. 11968–11979, Dec. 2021.

[8] Z. Zhu et al., "Torque-ripple-mitigated model-free predictive current control with extended control set for PMSMs," *IEEE Trans. Magn.*, vol. 60, no. 9, Sep. 2024, Art. no. 8203206, doi: 10.1109/TMAG.2024.3418982.

[9] Y. Zhang, J. Jin, and L. Huang, "Model-free predictive current control of PMSM drives based on extended state observer using ultralocal model," *IEEE Trans. Ind. Electron.*, vol. 68, no. 2, pp. 993–1003, Feb. 2021.

[10] J. Zhao, Y. Zhang, and X. Wang, "Model-free predictive current control of PMSM drives based on variable sequence space vector modulation using an ultra-local model," *IEEE Trans. Transp. Electrific.*, vol. 10, no. 2, pp. 3518–3528, Jun. 2024.

[11] Y. Zhou, H. Li, R. Liu, and J. Mao, "Continuous voltage vector model-free predictive current control of surface mounted permanent magnet synchronous motor," *IEEE Trans. Energy Convers.*, vol. 34, no. 2, pp. 899–908, Jun. 2019.

[12] Y. Wei, D. Ke, X. Yu, F. Wang, and J. Rodríguez, "Adaptive inertia observer-based model-free predictive current control for PMSM driving system of electric vehicles," *IEEE Trans. Ind. Appl.*, vol. 60, no. 4, pp. 6252–6262, Jul./Aug. 2024, doi: 10.1109/TIA.2024.3396123.

[13] J. Chen, Y. Fan, M. Cheng, Q. Zhang, and Q. Chen, "Parameter-free ultralocal model-based deadbeat predictive current control for PMVMs using finite-time gradient method," *IEEE Trans. Ind. Electron.*, vol. 70, no. 6, pp. 5549–5559, 2023.

[14] Z. Yin, X. Wang, X. Su, Y. Shen, D. Xiao, and H. Zhao, "A switched ultra-local model-free predictive controller for PMSMs," *IEEE Trans. Power Electron.*, vol. 39, no. 9, pp. 10665–10669, Sep. 2024, doi: 10.1109/TPEL.2024.3399599.

[15] M. Yang et al., "Multi-vector-based model-free predictive speed control with disturbance suppression and weighting factor elimination for SPMSM," *IEEE Trans. Transp. Electrific.*, to be published, doi: 10.1109/TTE.2024.3410529.

[16] Y. Wei, H. Young, F. Wang, and J. Rodríguez, "Generalized data-driven model-free predictive control for electrical drive systems," *IEEE Trans. Ind. Electron.*, vol. 70, no. 8, pp. 7642–7652, Aug. 2023.

[17] Y. Wei, H. Young, D. Ke, F. Wang, H. Qi, and J. Rodríguez, "Model-free predictive control using sinusoidal generalized universal model for PMSM drives," *IEEE Trans. Ind. Electron.*, vol. 71, no. 11, pp. 13720–13731, Nov. 2024, doi: 10.1109/TIE.2024.3379667.

[18] Y. Wei, H. Young, D. Ke, F. Wang, and J. Rodríguez, "Model-free predictive current control using extended affine ultralocal for PMSM drives," *IEEE Trans. Ind. Electron.*, vol. 71, no. 7, pp. 6719–6729, Jul. 2024, doi: 10.1109/TIE.2023.3314914.

[19] F. Wang, Y. Wei, H. Young, D. Ke, D. Huang, and J. Rodríguez, "Continuous-control-set model-free predictive control using time-series subspace for PMSM drives," *IEEE Trans. Ind. Electron.*, vol. 71, no. 7, pp. 6656–6666, Jul. 2024, doi: 10.1109/TIE.2023.3310017.

[20] J. Li, Y. Xia, X. Qi, and Z. Gao, "On the necessity, scheme, and basis of the linear–nonlinear switching in active disturbance rejection control," *IEEE Trans. Ind. Electron.*, vol. 64, no. 2, pp. 1425–1435, Feb. 2017.

[21] X. Zhang, C. Zhang, Z. Wang, and J. Rodríguez, "Motor-parameter-free model predictive current control for PMSM drives," *IEEE Trans. Ind. Electron.*, vol. 71, no. 6, pp. 5443–5452, Jun. 2024.

[22] X. Yuan, Y. Zuo, Y. Fan, and C. H. T. Lee, "Model-free predictive current control of SPMSM drives using extended state observer," *IEEE Trans. Ind. Electron.*, vol. 69, no. 7, pp. 6540–6550, Jul. 2022.

[23] X. Wu, J. Kang, M. Yang, T. Wu, and S. Huang, "Model-free deadbeat predictive current control for SPMSM based on adaptive gain extended state observer," *IEEE Trans. Transp. Electrific.*, to be published, doi: 10.1109/TTE.2024.3392907.

[24] X. Wu et al., "Model-free predictive current control of SPMSM based on enhanced extended state observer," *IEEE Trans. Ind. Electron.*, vol. 71, no. 4, pp. 3461–3471, Apr. 2024.

[25] J. Lee, H. Seo, J. -S. Lee, B. -K. Han, and H. -S. Mok, "Electrical parameter estimation method for surface-mounted permanent magnet synchronous motors considering voltage source inverter nonlinearity," *IEEE Access*, vol. 11, pp. 16288–16296, 2023.

[26] K. D. Hoang and H. K. A. Aorith, "Online control of IPMSM drives for traction applications considering machine parameter and inverter nonlinearities," *IEEE Trans. Transp. Electrific.*, vol. 1, no. 4, pp. 312–325, Dec. 2015.

[27] K. Liu and Z. Q. Zhu, "Online estimation of the rotor flux linkage and voltage-source inverter nonlinearity in permanent magnet synchronous machine drives," *IEEE Trans. Power Electron.*, vol. 29, no. 1, pp. 418–427, Jan. 2014.

[28] D. -M. Park and K. -H. Kim, "Parameter-independent online compensation scheme for dead time and inverter nonlinearity in IPMSM drive through waveform analysis," *IEEE Trans. Ind. Electron.*, vol. 61, no. 2, pp. 701–707, Feb. 2014.

[29] O. Babayomi, Z. Zhang, Z. Li, M. L. Heldwein, and J. Rodriguez, "Robust predictive control of grid-connected converters: Sensor noise suppression with parallel-cascade extended state observer," *IEEE Trans. Ind. Electron.*, vol. 71, no. 4, pp. 3728–3740, Apr. 2024.

[30] O. Babayomi and Z. Zhang, "Model-free predictive control of power converters with multifrequency extended state observers," *IEEE Trans. Ind. Electron.*, vol. 70, no. 11, pp. 11379–11389, Nov. 2023.

[31] O. Babayomi and Z. Zhang, "Model-free predictive control of power converters with cascade-parallel extended state observers," *IEEE Trans. Ind. Electron.*, vol. 70, no. 10, pp. 10215–10226, Oct. 2023.

[32] W. Xu, R. Dian, Y. Liu, D. Hu, and J. Zhu, "Robust flux estimation method for linear induction motors based on improved extended state observers," *IEEE Trans. Power Electron.*, vol. 34, no. 5, pp. 4628–4640, May 2019.

[33] M. Zhao, Z. Liu, Q. Chen, G. Liu, X. Zhu, and C. H. T. Lee, "Frequency adaptive disturbance observer for sensorless control of a 3 × 3-phase PMA-SynRM driven by mono-inverter," *IEEE Trans. Power Electron.*, vol. 38, no. 12, pp. 15314–15326, Dec. 2023.

[34] H. -S. Kim, K. -H. Kim, and M. -J. Youn, "On-line dead-time compensation method based on time delay control," *IEEE Trans. Control Syst. Technol.*, vol. 11, no. 2, pp. 279–285, Mar. 2003.

[35] X. Wu, B. Chen, M. Yang, T. Wu, S. Huang, and H. Cui, "Improved model-free predictive current control method for SPMSM with an overmodulation scheme," *IEEE Trans. Ind. Electron.*, vol. 71, no. 8, pp. 8427–8437, Aug. 2024, doi: 10.1109/TIE.2023.3317855.

Zixuan Liu (Student Member, IEEE) was born in Zhejiang Province, China, in 1998. He received the B.Eng. degree in electrical engineering in 2021 from Zhejiang University, Hangzhou, China, where he is currently working toward the Ph.D. degree in electrical engineering.

His research interests include electrical machines and their control systems, and PM machine drives.

Xiaoyan Huang (Member, IEEE) received the B.E. degree in control measurement techniques and instrumentation from Zhejiang University, Hangzhou, China, in 2003, and the Ph.D. degree in electrical machines and drives from the University of Nottingham, Nottingham, U.K., in 2008.

She is currently a Professor with the College of Electrical Engineering, Zhejiang University, where she is working on electrical machines and drives.

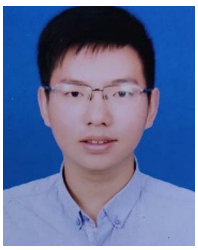

Qichao Hu was born in Zhejiang, China, 1999. He received the B.E. degree in electrical engineering in 2021 from Zhejiang University, Hangzhou, China, where he is currently working toward the M.S. degree in electric machines and electric apparatus.

His research interests include high-performance control methods for servo motors.

Geng Yang (Member, IEEE) received the B.Eng. and M.Sc. degrees in instrument science and engineering from the College of Biomedical Engineering and Instrument Science, Zhejiang University, Hangzhou, China, in 2003 and 2006, respectively, and the Ph.D. degree in electronic and computer systems from the Department of Electronic and Computer Systems, Royal Institute of Technology, Stockholm, Sweden, in 2013.

Yunchong Wang (Member, IEEE) was born in Liaoning, China, in 1987. He received the B.S. and M.S. degrees from Zhejiang University, Hangzhou, China, in 2010 and 2013, respectively, and the Ph.D. degree from the Hong Kong Polytechnic University, Hong Kong, in 2017, all in electrical engineering.

Since 2020, he has been an Associate Professor of electrical engineering with Zhejiang University. He has authored more than 30 technical papers. His research interests include the design and control of permanent magnet machines, novel electrical motors for electrical vehicles, hybrid electrical vehicles, and renewable energy conversion systems.

Jianxin Shen (Senior Member, IEEE) was born in Huzhou, China, in 1969. He received the B.Eng. and M.Sc. degrees from Xi'an Jiaotong University, Xi'an, China, in 1991 and 1994, respectively, and the Ph.D. degree from Zhejiang University, Hangzhou, China, in 1997, all in electrical engineering.

From 1997 to 1999, he was with Nanyang Technological University, Singapore. From 1999 to 2002, he was with the University of Sheffield, Sheffield, U.K. From 2002 to 2004, he was with the IMRA Europe SAS, U.K. Research Centre, Brighton, U.K. Since 2004, he has been a Professor of electrical engineering with Zhejiang University. He has authored more than 320 technical papers. He holds more than 40 patents. His main research interests include topologies, control and applications of permanent magnet machines and drives, and renewable energies.